Charge-Transfer and *dd* excitations in AgF_2

Nimrod Bachar,[1,*] Kacper Koteras,[2] Jakub Gawraczynski,[2] Waldemar Trzciński,[3] Józef Paszula,[3] Riccardo Piombo,[4] Paolo Barone,[5] Zoran Mazej,[6] Giacomo Ghiringhelli,[7,8] Abhishek Nag,[9] Ke-Jin Zhou,[9] José Lorenzana,[10,†] Dirk van der Marel,[1] and Wojciech Grochala[2]

[1]*Department of Quantum Matter Physics, University of Geneva, CH-1211 Geneva 4, Switzerland*
[2]*Center of New Technologies, University of Warsaw, Żwirki i Wigury 93, 02-089 Warsaw, Poland*
[3]*Department of New Technologies and Chemistry, Military University of Technology, gen. Sylwestra Kaliskiego 2, 00-908 Warsaw, Poland*
[4]*Dipartimento di Fisica, Università di Roma "La Sapienza", 00185 Rome, Italy*
[5]*Superconducting and Other Innovative Materials and Devices Institute (SPIN), Consiglio Nazionale delle Ricerche, Area della Ricerca di Tor Vergata, Via del Fosso del Cavaliere 100, I-00133 Rome, Italy*
[6]*Department of Inorganic Chemistry and Technology, Jožef Stefan Institute, Jamova cesta 39, 1000 Ljubljana, Slovenia*
[7]*Dipartimento di Fisica, Politecnico di Milano, piazza Leonardo da Vinci 32, 20133 Milan, Italy*
[8]*CNR-SPIN, Dipartimento di Fisica, Politecnico di Milano, piazza Leonardo da Vinci 32, 20133 Milan, Italy*
[9]*Diamond Light Source, Harwell Campus, Didcot OX11 0DE, United Kingdom*
[10]*Institute for Complex Systems (ISC), Consiglio Nazionale delle Ricerche, Dipartimento di Fisica, Università di Roma "La Sapienza", 00185 Rome, Italy*

(Received 20 June 2021; accepted 5 April 2022; published 9 May 2022; corrected 20 July 2022)

Charge-transfer insulators are the parent phase of a large group of today's unconventional high-temperature superconductors. Here we study experimentally and theoretically the interband excitations of the charge-transfer insulator silver fluoride AgF_2, which has been proposed as an excellent analog of oxocuprates. Optical conductivity and resonant inelastic x-ray scattering on AgF_2 polycrystalline sample show a close similarity with that measured on undoped La_2CuO_4. While the former shows a charge-transfer gap ∼3.4 eV, larger than in the cuprate, *dd* excitations are nearly at the same energy in the two materials. Density functional theory and exact diagonalization cluster computations of the multiplet spectra show that AgF_2 is more covalent than the cuprate, in spite of the larger fundamental gap. Furthermore, we show that AgF_2 is at the verge of a charge-transfer instability. The overall resemblance of our data on AgF_2 to those published previously on La_2CuO_4 suggests that the underlying charge-transfer insulator physics is the same, while AgF_2 could also benefit from a proximity to a charge density wave phase as in $BaBiO_3$. Therefore, our work provides a compelling support to the future use of fluoroargentates for materials' engineering of novel high-temperature superconductors.

DOI: 10.1103/PhysRevResearch.4.023108

I. INTRODUCTION

Following the discovery of a high-T_c superconductivity in the cuprate oxide (CuO) family, there has been an ongoing search for other systems in which it will be possible to replicate such novel properties. Apart from purely fundamental research into the underlying physics of the unconventional superconducting state, there has also been the goal to find T_c at higher temperatures.

In most cases, the key players of this approach were elements originating, such as copper, from the transition-metal group of the periodic table, and over time several candidates came into focus such as iridates, nickelates, and vanadates. The vanadates [1,2] appear to be extremely resilient to external doping [3] unlike the various compounds of the cuprate family. Superconductivity under doping was predicted theoretically in iridates [4], which are isostructural to the cuprates and share several similarities with the properties of the antiferromagnetic (AFM) phase. However, there are some distinct differences compared to the cuprates. First, there is a strong competition between electronic correlations, spin-orbit coupling, and crystal field energy scales in the iridates. Second, Sr_2IrO_4 is a Mott insulator [5], while La_2CuO_4 is a charge-transfer (CT) insulator. Extensive experimental studies via various doping approaches did not result in any signatures for superconducting properties even upon heavy doping levels, as in the $La_{2-x}Sr_xIrO_4$ compound [5–7]. Quite interestingly, although $NdNiO_3$ has neither the AFM ground state nor the strong covalent bonding commonly found in cuprates, Sr-doped $NdNiO_2$ exhibits low-temperature superconductivity in an infinite layer structure as was shown recently [8].

There is, however, another approach to replace copper, and that is by staying in the same column of the periodic table of elements and by choosing silver. It was already clear from the early stages of that paradigm that silver oxide cannot become

*Present address: Department of Physics, Faculty of Natural Sciences, Ariel University, Ariel; nimib@ariel.ac.il
†jose.lorenzana@uniroma1.it

a true charge-transfer insulator because of the high second ionization energy of silver and the fact that oxygen is not a sufficiently electronegative element [9]. As a result, AgO has a negative charge-transfer energy that ends up in the Ag^{1+} oxidation state without a magnetic ordering as opposed to its sibling, CuO. Fluorine is more electronegative than oxygen, therefore has deeper $2p^6$ states, which results in a positive charge-transfer energy. Several fluoroargentates were found to be isoelectronic to their cuprate sibling La_2CuO_4. However, previous work showed that their magnetic ground state is not the same as, for example, in the case of Cs_2AgF_4 [10] and K_2AgF_4, both being ferromagnetic [11], with small local structural distortions of the AgF_6 octahedron stabilizing an antiferro orbital ordering [12].

Recent calculations predict that the magnetic ground state of $KAgF_3$ and AgF_2 is AFM. $KAgF_3$ has an arrangement of spins within the zigzag chain along the crystallographic c-axis direction forming an AFM with a low-temperature Néel transition and a theoretical gap of 0.7 eV [11,13]. However, its quasi-one-dimensional (quasi-1D) magnetic structure cannot be compared directly with the quasi-2D AFM state of the cuprates. On the other hand, AgF_2 has a neutral-plane stacked structure due to the inherent F^- character (instead of O^{2-} in CuO_2), although with strongly buckled planes. Therefore, AgF_2 is the equivalent "012" (free-of-charge reservoir layer) of the 214 stoichiometry in cuprates [11,14]. The Néel temperature of AgF_2 ($T_N = 163$ K) is half of that for La_2CuO_4 ($T_N = 325$ K). LSDA + U calculations predicted a gap of 1.5–2.5 eV in various forms of AgF_2 [15–17]. Hybrid density functional theory calculations involving orbital character demonstrated the striking resemblance of the electronic structure of AgF_2 and its cuprate analog La_2CuO_4 [14]. Furthermore it predicted also the exchange energy J to be about 70 meV in AgF_2 [14,17], half of the J value in typical cuprate compounds. A one-to-one comparison of the two-magnon excitation in Raman spectroscopy data of AgF_2 and $EuBa_2Cu_3O_6$ confirmed the expected J of about 70 meV in AgF_2 [14]. Although the charge-transfer gap between the F $2p$ state and the Ag $4d$ state was predicted in previous theoretical calculations, a direct experimental verification of the high-energy electronic excitations in AgF_2 is still lacking [11,14]. In that respect, optical spectroscopy is an unprecedented method for determining intraband and interband transitions, which proved to be of most importance in the study of doped charge transfer and Mott insulator systems. Moreover, resonant inelastic x-ray scattering (RIXS) has been exploited in the past decade to study core and valence excitations of cuprates, thus providing novel and exciting observations of electronic dd and charge-transfer excitations along with collective excitations such as bimagnons [18] and charge density waves [19]. Therefore, not only are the latter two spectroscopy techniques essential in verifying the electronic character of argentates, but they act as a direct tool to do so in order to compare them exclusively with previous theoretical predictions or future and further study of these cupratelike compounds. As we will see, the current study sheds light on previous predictions and gives new insight regarding the charge-transfer physics in argentates.

In this work, we study the high-energy excitations of AgF_2 by combining optical spectroscopy and resonant inelastic x-ray scattering. The excitation spectrum is compared with cluster computation aided with DFT computation of parameters. We show that the optical conductivity spectrum close to the charge-transfer gap resembles that of the oxocuprates and contradicts previous band-gap estimations in AgF_2. In addition, we identified several dd excitations in the RIXS spectra. Our experimental observations are supported by new theoretical calculations of the electronic excitations in AgF_2. The striking similarity between fluoroargentate and oxocuprates suggests that the former could be a promising candidate for a future high-T_c superconductor. Moreover, a close analysis of our results suggests that AgF_2 is at the border of a charge-transfer instability. Therefore, we suggest that AgF_2 is a novel and interesting test bed for further investigation of strong electronic correlations in quantum materials.

II. METHODS

A. Sample preparation

A 10 g batch of polycrystalline AgF_2 has been freshly prepared as described previously [14]. Purity of the obtained sample has been verified using powder x-ray diffraction testifying to the presence of minute amounts (approximately 1 wt %) of diamagnetic AgF only.

To obtain a compact specimen of AgF_2 for optical measurements, an explosion compaction procedure was applied as described in Appendix A. Sample cylinder was cut into approximately 2 mm thin hard compact wafers, which were fine polished inside the glove box using diamond paper before performing any optical measurements.

Samples were loaded inside the cryostat chamber using an inert gas-filled glove bag and with an active flow of gas, with a loading period of a few minutes, followed by evacuation of the sample chamber to ultrahigh vacuum (UHV). No visual changes of the sample surface could be seen, testifying the successful loading without any chemical deterioration of the sample.

B. Optical spectroscopy

The optical response of polished pressed powder AgF_2 samples was measured by combining infrared reflectivity and ellipsometry. The sample was installed in an UHV helium flow cryostat and data was recorded at selected temperatures from room temperature down to 8 K. The cryostat is designed to maintain a high position stability of the mounted sample during cool down. Measurements were obtained using a near normal incident reflectivity setup in a Bruker Vertex 70V Fourier transform infrared (FTIR) spectrometer in the photon energy range of approximately 3.5 meV to 0.6 eV. Calibration spectra were obtained by measuring a gold layer deposited on top of the sample using *in situ* thermal evaporation. In the photon energy range of 0.5–3.5 eV the complex dielectric function was determined using a Woollam VASE® spectroscopic ellipsometer. The ratios of the reflection coefficients for p and s polarized light $\rho = r_p/r_s$, were measured at incident angles of 61° and 63° (see Appendix B).

The optical conductivity was calculated directly from the pseudodielectric function using two sets of ellipsometry data at two different angles of incidence. In addition, we

have fitted the ellipsometry parameters, Ψ_{ellip} and Δ_{ellip} to the Drude-Lorentz parametrization to obtain boundaries for our confidence in the optical conductivity spectra. We have used the far-IR reflectivity data to obtain the contribution of phonons to the spectra. The fit to the lowest-energy phonon at about 30 cm^{-1} along with the fit to the ensemble of all far infrared (FIR) phonons were used to extrapolate the reflectivity to zero frequency. The frequency and temperature dependence of the real part of the optical conductivity will be discussed in Sec. III.

C. RIXS

A polycrystalline sample was mounted on a copper sample holder in an inert atmosphere inside a glove box, loaded in a vacuum suitcase, and transferred to the experimental chamber maintained at $\approx 5 \times 10^{-10}$ mbar. The F K-edge x-ray absorption (XAS) spectrum was collected in the fluorescence yield mode using σ polarization (normal to the scattering plane) at an angle of incidence of 75°. Resonant inelastic x-ray scattering (RIXS) spectra were collected at F K edge with an energy resolution of $\delta E \approx 0.045$ eV at a scattering angle of 150° at 13 K, at I21-RIXS beam line, Diamond Light Source, United Kingdom [20]. The zero-energy transfer position and energy resolution of the RIXS spectra were determined from subsequent measurements of elastic peaks from an adjacent carbon tape. The RIXS spectrum was collected with π polarization (parallel to the scattering plane) at 682.2 eV at an angle of incidence of 20° for 30 min. The RIXS spectrum was fitted with Gaussian line shapes for the elastic peak and phonons, with a damped harmonic oscillator model for the bimagnon, with Gaussian line shapes for the *dd* excitations and charge transfer excitation, and a fluorescence model [21] for the emission feature peaking around 5 eV. The incident energy map was collected at an angle of incidence of 20° and σ polarization. RIXS spectra comparison after 6 h of x-ray beam exposure showed only a reduction in the overall emission signal, with no noticeable difference in the intensity ratios of the inelastic features (not shown).

D. Theory

To model the AgF_2 electronic excitations with Ag in a formally d^9 state, we considered an $(AgF_6)^{4-}$ cluster reproducing the local environment of the transition-metal ion as shown in Fig. 1. The one-particle parameters were obtained from unpolarized DFT calculations of the periodic solid using the projector-augmented wave (PAW) method as implemented in VASP [22] within the generalized gradient approximation of Perdew, Burke, and Ernzerhof [23] (PBE) using a mesh of $8 \times 8 \times 8$ k points.

The band structure was obtained with the experimental lattice parameters of Ref. [24] and then projected onto maximally localized Wannier functions as implemented in the WANNIER90 code [25]. We used a Wannier basis with five d orbitals per Ag and three p orbitals per F. The two planar F-Ag-F bridges deviate slightly from orthogonality (93.3°). For the d orbitals, we took the axes so that the bisectrix of the axes coincides with the bisectrix of the bridges, resulting in

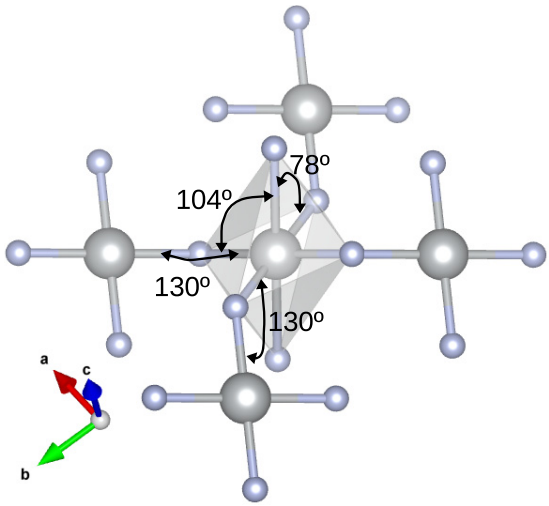

FIG. 1. The central gray octahedron shows the AgF_6 cluster used in the computations. The surrounding atoms are implicitly taken into account in the definition of diagonal energies. Some key bond angles are indicated for clarity.

axes nearly oriented along AgF bonds. For the p orbitals we used the local reference frame as in Ref. [14].

The WANNIER90 one-particle Hamiltonian for the solid was truncated to the AgF_6 cluster yielding a Hamiltonian with five d orbitals and $3 \times 6 = 18$ p orbitals. The one-particle Hamiltonian reads

$$\begin{aligned} H_{pd} = &\sum_{\nu} \varepsilon_d(\nu) d_\nu^\dagger d_\nu + \sum_{m} \varepsilon_p(m) p_m^\dagger p_m \\ &+ \sum_{\nu m} t_{pd}(\nu, m) d_\nu^\dagger p_m + \text{H.c.} \\ &+ \sum_{m m'} t_{pp}(m, m') p_m^\dagger p_{m'} + \text{H.c.}, \end{aligned} \tag{1}$$

where ν, m are spin-orbital indexes, $d_\nu^\dagger$ creates a hole in the d orbitals ($d_{3z^2-r^2}, d_{x^2-y^2}, d_{xy}, d_{xz}, d_{yz}$) while $p_m^\dagger$ creates a hole in one of the 18 p orbitals. We considered pd hopping across the six F-Ag bonds [$t_{pd}(\nu, m)$] and pp hopping across the 12 F-F bonds forming the edges of the octahedral cage [$t_{pp}(m, m')$]. Spin-orbit coupling was not included, so the spin is conserved.

The symmetry of the octahedra (Fig. 1) is quite low as inversion is the only nontrivial symmetry operation allowed (C_i point group). Therefore, the five d levels may have different energies and hybridization matrix elements among them are allowed. Notwithstanding that, we find that with the chosen axes, off-diagonal dd matrix elements on the Ag site are very small and were neglected.

Some linear combinations of p orbitals are nonbonding and can be eliminated to reduce the Hilbert space. To this aim, we defined five symmetry adapted orbitals by the following transformation:

$$\tilde{P}_\nu = \frac{1}{\sqrt{\tilde{T}_{pd}(\nu)}} \sum_m t_{pd}(\nu, m) p_m$$

TABLE I. Crystal fields and hybridizations obtained from DFT and Wannier computations. All values are in eV. The diagonal energies of P orbitals in Eq. (2) are determined by $\varepsilon_P(\nu) = \Delta + e_P(\nu)$. The value for Δ obtained this why is $\Delta_{\rm DFT} = 1.29$ eV but a different value can be used to study the effect of increased ionicity. The last column are the expressions for the hybridizations in terms of the x^2-y^2 matrix element and for a planar D_{4h} cluster used by Eskes *et al.* [26].

	AgF_2 (C_i)			La_2CuO_4	(D_{4h})
ν	$\varepsilon_d(\nu)$	$e_P(\nu)$	$T_{pd}(\nu)$	$\varepsilon_d(\nu)$	$e_P(\nu)$	$T_{pd}(\nu)$
z^2	−0.25	0.32	1.51	0	$\frac{4}{5}T_{pp}$	$\frac{1}{\sqrt{3}}T_{pd}$ [a]
x^2-y^2	−0.28	−0.16	2.76	0	$-\frac{6}{5}T_{pp}$	T_{pd} [a]
xy	0.34	−0.05	1.36	0	$\frac{4}{5}T_{pp}$	$\frac{1}{2}T_{pd}$ [a]
xz	0.09	−0.14	1.05	0	$-\frac{1}{5}T_{pp}$	$\frac{1}{2\sqrt{2}}T_{pd}$ [a]
yz	0.10	0.04	1.02	0	$-\frac{1}{5}T_{pp}$	$\frac{1}{2\sqrt{2}}T_{pd}$ [a]

[a](x^2-y^2) symmetry.

with

$$\tilde{T}_{pd}(\nu) = \sqrt{\sum_m |t_{pd}(\nu, m)|^2}.$$

This defines a set of orbitals with maximum overlap with the d orbitals. Because of the low symmetry, the resulting orbitals are not orthogonal but are easily orthogonalized, resulting in new operators P_ν and hybridization matrix elements $T_{pd}(\nu)$, which expand the same maximally hybridized subspace. The orthogonalized orbitals (hereafter P orbitals) have nearly the same symmetry as the original orbitals, so they can still be labeled as x^2-y^2, xy, etc. Furthermore, they have small interorbital PP and Pd matrix elements between orbitals of different symmetry. We checked that keeping these matrix elements did not change the results significantly, therefore for simplicity they were also neglected.

The resulting Hamiltonian of the $(AgF_6)^{4-}$ cluster reads

$$\begin{aligned} H = &\sum_\nu \varepsilon_d(\nu) d_\nu^\dagger d_\nu + \sum_\nu \varepsilon_P(\nu) P_\nu^\dagger P_\nu \\ &+ \sum_\nu T_{pd}(\nu)(d_\nu^\dagger P_\nu + P_\nu^\dagger d_\nu) \\ &+ \sum_{\substack{\nu_1,\nu_2 \\ \nu_3,\nu_4}} U^{(dd)}(\nu_1,\nu_2,\nu_3,\nu_4) d_{\nu_1}^\dagger d_{\nu_2}^\dagger d_{\nu_3} d_{\nu_4}. \end{aligned} \tag{2}$$

Table I shows the one-body parameters deduced from the WANNIER90 computation. Setting $T_{pd}(x^2-y^2) = 2.76$ eV, the values of the $T_{pd}(\nu)$ matrix elements are in very good agreement with the expressions [26] for a cluster with D_{4h} symmetry using a Slater-Koster parametrization and assuming $T_{pd}(xy) = T_{pd}(x^2-y^2)/2$ (last column of Table I). The symmetrized P orbitals manifest a more evident deviation of square planar symmetry, and the D_{4h} expressions for $e_P(\nu)$ are not accurate.

We define the charge-transfer parameter $\Delta = E(d^{10}\underline{L}) - E(d^9)$ where $\underline{L}$ denotes a hole in the ligand and the energies are average of the indicated multiplets setting $T_{pd}(\nu) = 0$. Interactions with the neighboring atoms are absorbed in the definition of Δ. In the case of intracluster excitations in the insulating phase, we need to consider one hole in the cluster, making the interaction term in Eq. (2) irrelevant. The full Hamiltonian will become relevant for intercluster excitations.

III. RESULTS

A. Optical conductivity

The real part of the optical conductivity, σ_1, of the AgF_2 sample for selected temperatures is shown in Fig. 2. The spectra can be divided into several regimes and their equivalent excitations: far-IR phonons (seen as red sharp peaks), mid-IR absorption (above 0.1 eV), and near-IR to ultraviolet (UV) absorption. The former two low-energy excitations will be discussed in a separate publication. The high-energy spectrum (Fig. 2) can be decomposed into three major excitations. The strongest one is the high-energy absorption centered at about 3.4 eV with an onset at approximately 1.75 eV. This absorption can be associated with a strong interband transition, which sits at energies close to our experimental data range limit.

In addition to the absorption tail of the this excitation, we detect a broad absorption band, which can be roughly decomposed into two modes centered at around 1 eV and 1.7 eV. As the sample is warmed up to room temperature, the 1.7 eV excitation seems to remain almost intact with respect to energy, while the 1 eV excitation seems to soften toward 0.8 eV. The two separate modes can be easily distinguished in the spectra measured at 300 K as shown in Fig. 2. As will be seen below, the excitation at 3.4 eV and the optical mode at 1.7 eV are consistent with a charge-transfer excitation and dd excitations, respectively, as seen in the RIXS data. We also note a possible spectral weight transfer from the high-energy sector to the subgap excitations as a function of temperature and as shown in Fig. 2. However, the confidence boundary that we have on our optical conductivity data in this range requires a further and more precise experimental investigation of this range to understand this spectral weight interplay as a function of temperature. Further discussion of the optical conductivity spectra and comparison with that of the cuprate analog La_2CuO_4 (black line) will be given in Sec. IV A.

B. X-ray absorption

Figure 3 (top panel) shows the F K-XAS on AgF_2. We attribute the edge and the sharp peak marked by the arrow (682 eV) to excitations into Ag 4d orbitals via hybridization with F 2p orbitals, reflecting the narrow UHB in AgF_2 [14]. This is justified by the fact that similar p-d hybridized peaks have been observed in F K-XAS of several 3d metal fluorides [30–32]. Further support for this interpretation comes from the similarity with the O K-XAS on La_2CuO_4 [29] (black line) to be discussed in Sec. IV B.

The broad absorption structure picking at 689 eV is assigned to Ag 5s and 5p states, which hybridize with F-2p states. These assignments are supported by the DFT computations shown in the bottom panel to be discussed in Sec. IV C.

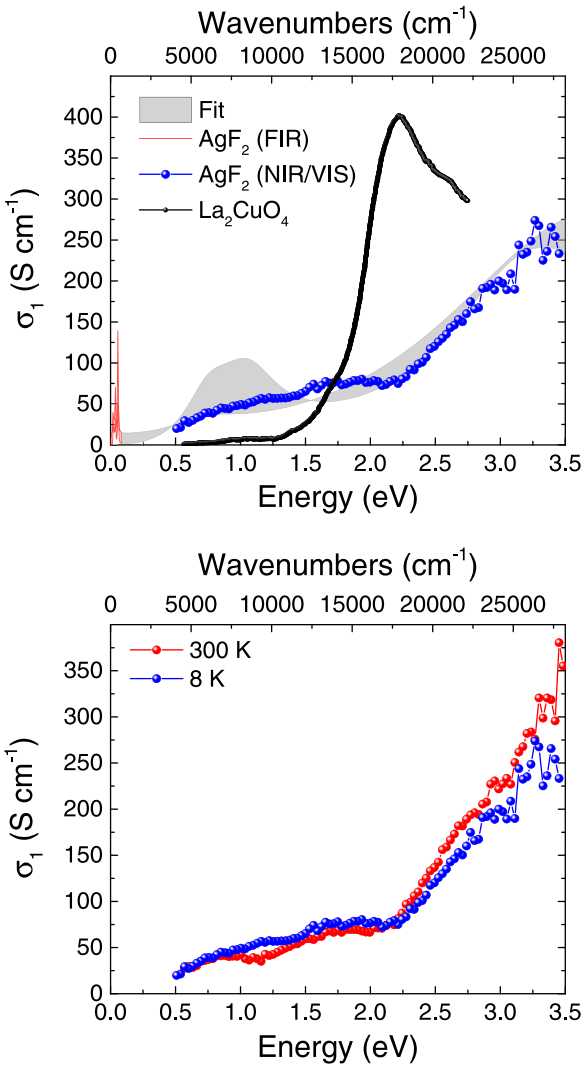

FIG. 2. Real part of optical conductivity for AgF_2 (this work). The top panel presents σ_1 (blue line with circles) as obtained from direct calculation of the pseudodielectric function using ellipsometry parameters Ψ_{ellip} and Δ_{ellip} for two angles of incidence as measured at a base temperature of 8 K. σ_1 as was obtained by near normal incidence reflectivity measurements in the far infrared is shown in red. The shaded gray area represents the result of a fit to Ψ_{ellip} and Δ_{ellip} data separately (see Appendix B), which reflects the confidence boundaries of our model with respect to the experimental data. Our data is compared with optical conductivity data adopted from Falck *et al.* [27,28] on undoped La_2CuO_4. The optical conductivity in the AgF_2 sample shows an onset at about 1.75 eV with high-energy band transition associated with the charge-transfer gap ($\Delta_{peak} \approx 3.4$ eV). The data on AgF_2 is compared with a charge-transfer excitation peaking at $\Delta_{peak} \approx 2.2$ eV with an onset of ≈1.6 eV in the equivalent oxocuprates compound La_2CuO_4. In addition, the AgF_2 data shows a low spectral weight subgap absorption suggesting negligible doping as intended [28]. Bottom panel shows a comparison with data at 300 K showing slight modifications of the different excitations in the charge-transfer sector and the subgap sector.

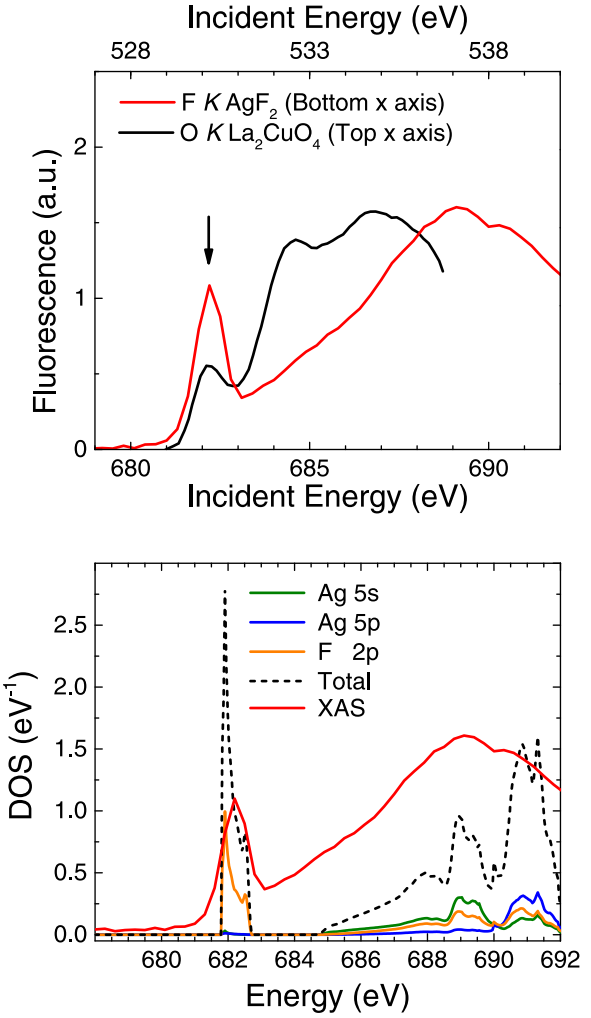

FIG. 3. Top panel: Comparison of F *K*-XAS on AgF_2 and O *K*-XAS on La_2CuO_4 [29]. AgF_2 and La_2CuO_4 XAS energies correspond to the bottom and the top *x* axes, respectively. Bottom panel: Orbital projected unoccupied density of states (DOS) of AgF_2 from the unpolarized DFT computations. The Fermi level has been shifted to 681.8 eV to facilitate comparison with F *K*-XAS (red line). The total unoccupied DOS, includes contributions from the shown symmetries above the edge as well as Ag 4*d*, which will be shown later [Fig. 5(a)]. For the band at the Fermi level, it is nearly equal to the difference of the total and F 2p contribution.

C. Resonant inelastic x-ray scattering

Upon excitation at the F K edge, a well-resolved RIXS spectrum can be observed (Fig. 4). In the insets of the middle panel in Fig. 4, we show that the low-energy part of the AgF_2 spectrum can be decomposed into an elastic peak (0 eV), phonons (0.041 eV) and their overtones, and a damped bimagnon peak (centered at 0.218 eV). The energy of the assigned bimagnon peak corresponds to that observed in the Raman spectra (∼3*J*) [14]. Bimagnons can be probed also with K-edge RIXS. However, to accurately determine the spectral contributions of the phonon progression and the bimagnon peak in AgF_2, momentum-resolved RIXS is desirable.

As shown in Fig. 4 (middle panel) a series of excitations at 1.59, 1.86, and 2.33 eV is observed, an assignment which will be substantiated below. At high energies (>4 eV), the RIXS spectrum is dominated by a broad feature with a strong resonance behavior as a function of the incident energy. We

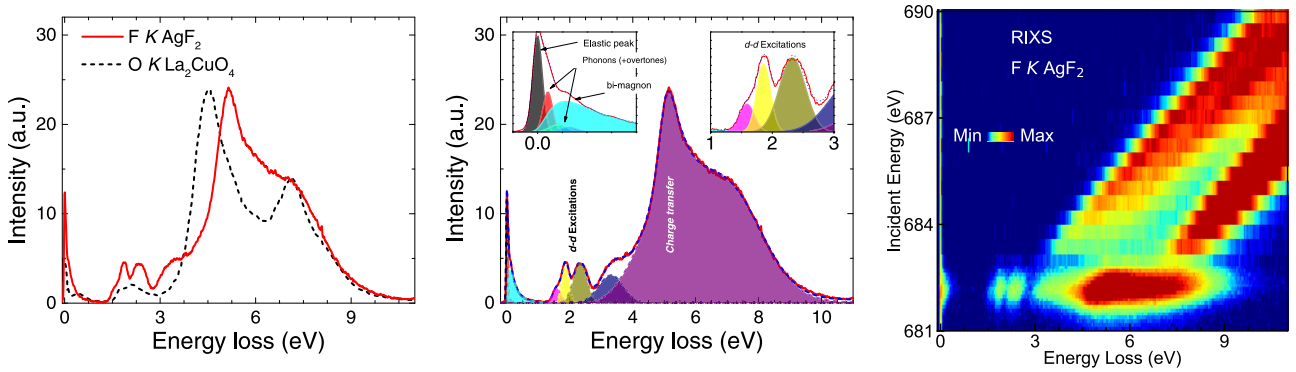

FIG. 4. Left panel: Comparison of F K-RIXS on AgF_2 and O K-RIXS on La_2CuO_4 [33]. Middle panel: F K-RIXS on AgF_2 fitted with multiple components: black, elastic peak; red, green, and blue, phonons and their overtones; cyan, bimagnon; magenta, yellow, and dark yellow, dd excitations; navy and purple, charge-transfer excitations (see text for further description). Insets show the low-energy inelastic features and dd excitations with fitted profiles in different colors as noted before. Right panel: F K-RIXS incident energy map on AgF_2 showing Raman and fluorescence features.

attribute the resonance to the excitation of charge-transfer transitions involving an Ag site and its neighboring F's as will be also explained below. Between the pd and the dd excitations, a peak is observed at 3.32 eV. The energy scale of this peak matches reasonably well with the growing optical conductivity of AgF_2 shown in Fig. 2. As such, this peak can be assigned to transitions across the charge-transfer gap from an Ag site to more distant F's and provides supporting evidence for the existence of a large fundamental gap in AgF_2. In fact, our current experimental observations contradict the previous predictions of the charge-transfer gap as reported in Ref. [14]. Both the dd and charge-transfer excitations are discussed in detail below while a further discussion of the comparison with the RIXS data of La_2CuO_4 will be given in Sec. IV B.

The map in Fig. 4 (right panel) shows energy-detuned RIXS spectra collected across the F K-XAS. Energy-detuned RIXS is very useful for revealing the degree of localization of the excitations. At higher incident photon energies (>683 eV), two fluorescence emission lines arise. We can view the fluorescence RIXS as an incoherent process, that is, the excitation and deexcitation are decoupled from each other. Electrons are excited from F 1s core level to unoccupied states involving Ag 5s, Ag 5p, and F 2p (cf. Fig. 3, bottom panel). The deexcitation is from the broad valence states to refill the 1s core hole resulting in a characteristic emission energy. In other words, the energy loss of fluorescence varies linearly with the incident energy. Across the resonance of the UHB peak (682.2 eV), dd and charge-transfer excitations resonate at the UHB peak and show an almost fixed energy loss, i.e., Raman-like, indicating the energy loss corresponds to the energy of fixed-number-of-particle excitations (i.e., excitons, particle-hole, etc.). The localized dd and charge-transfer excitations are widespread in many transition-metal oxides (including oxocuprates).

IV. DISCUSSION

A. Optical conductivity of AgF_2 vs. La_2CuO_4

We now turn back to the absorption spectrum as seen in the optical conductivity data shown in Fig. 2. Similar behavior of a high-energy absorption was well studied, in particular in the parent compound La_2CuO_4 [27,34]. In that case, a strong peak can be seen in the real part of the optical conductivity at about 2.2 eV [27,34,35] as we demonstrate in Fig. 2. The strong peak at 2.2 eV in La_2CuO_4 is associated with the charge-transfer transition between the O p band and Cu d band and was measured in various parent compounds of the cuprates family [35,36]. Taking into account the resemblance of the experimental data between AgF_2 and La_2CuO_4 with the supporting results of the theoretical analysis and the RIXS data, we associate the strong high-energy absorption in our data to the charge transfer excitation between the F p band to the Ag d band.

The broad tail down to 1.25 eV in the optical conductivity data of the AgF_2 sample, is similar but with a much weaker absorption to the tail in the optical conductivity data that was already reported in previous works regarding the cuprates [28,34,35,37–39] and as we reproduce in Fig. 2. Uchida *et al.* [34] demonstrated the appearance of a midinfrared (MIR) absorption depicted as a subgap peak centered at about 0.5 eV in the real part of the optical conductivity of Sr-doped La_2CuO_4. Falck *et al.* [28] showed that oxygen doping in $La_2CuO_{4+\delta}$ results in a similar MIR absorption, which is dominant in sample with $\delta = 0.014$ and reduced T_N of 250 K. On the other hand, in an undoped sample with $\delta = 0$ and $T_N = 322$ K the MIR absorption is negligible as can be seen in Ref. [28]. The MIR band, which appears as a peak in the real part of the optical conductivity of doped samples, partially draws spectral weight from a higher energy range, thus diminishes the charge-transfer excitation upon further doping [34]. The intensity of the MIR band is of the order of the charge-transfer excitation in nearly undoped La_2CuO_4 and even stronger for intermediate doping levels [28,34]. Since we detect a MIR-NIR absorption band, which is weak compared to that of the charge-transfer excitation, we conclude that the AgF_2 is practically in its undoped phase, as intended.

B. AgF_2 vs. La_2CuO_4 from XAS and RIXS

In Fig. 3 (top panel) we compare F K-XAS in AgF_2 to O K-XAS in La_2CuO_4 [29]. The peak at the absorption threshold of

La_2CuO_4 reflects the O $2p$-Cu $3d$ hybridization and originates upon excitation to the upper Hubbard band (UHB) of predominantly $3d_{x^2-y^2}$ character in this material [29]. The broad structures ranging from ∼ 531–537 eV reflect hybridizations between unoccupied O $2p$ and La $5d$ and $4f$ DOS. In AgF_2 there are no ions playing the role of La, so a different explanation for the broad absorption is needed (see below).

As an additional comparison, O K-RIXS spectrum of La_2CuO_4 is also presented in Fig. 4 (left panel). The low-energy excitations around 2 eV resemble the well-known dd excitations of cuprates [33]. The bimagnon excitation at 0.218 eV of the AgF_2 sample is similar to that which is observed in the O K-RIXS on La_2CuO_4 in the MIR region [33]. Therefore, the RIXS data of AgF_2 and La_2CuO_4 shows an overall remarkable similarity, which facilitates the assignment of the different features noted above and further supports the claim that silver fluorides are excellent cuprate analogs. Additional information can be learned from the comparison of cluster calculation results between the two families, which will be presented in Sec. IV D.

C. Comparison with density functional theory computations

1. X-ray absorption

In the x-ray absorption process, a core electron is excited to the unoccupied F states. Thus, the F-projected unoccupied DOS from DFT provides a first approximation to the spectra. Figure 3 (bottom panel) shows that there is a good match with the main structures observed. As anticipated, the DFT computations show that the broad absorption can be assigned to Ag $5s$ and $5p$ states. Notice that the F $2p$ projected DOS has large intensity at the position of both, $5s$ and $5p$ states, which testify for the strong hybridization.

The peak near 682 eV is, as explained above, attributed to the upper Hubbard band states, which have mainly Ag-$4d$ character but are strongly mixed with F-$2p$ states. The weight of the $4d$ states in this region is approximately given by the difference between the total and the F-$2p$ DOS, which is somewhat larger than the F-$2p$ weight and again indicates strong hybridization.

2. Assignment of dd transitions

Figure 5 (top panel) shows the local DOS from DFT computations, projected on the different d-orbital symmetry in the nonmagnetic (metallic) solution with the abscissa origin now set at the Fermi energy. Due to the stronger hybridization compared to other symmetries (cf. Table I), the antibonding $d_{x^2-y^2}$ band is half-filled and is well separated from the other (filled) d bands. Figure 5(b) shows the joint DOS between the unoccupied $d_{x^2-y^2}$ and occupied orbitals of the other symmetries, representing dd transitions with a constant matrix element. Averaging over the four possible final states (black line), one obtains a line shape surprisingly similar in position and overall shape to the dd RIXS spectra, despite neglecting matrix element effects. The theoretical line shape is broader than the experiment, which can be attributed to correlation-induced band narrowing effects absent in DFT. Neglecting minor differences, this analysis allows assigning the lower shoulder to transitions of the $d_{x^2-y^2}$ hole to z^2 orbitals, the higher peak to transitions to mainly xz orbitals and the intermediate band to a mixed character. Such assignments are in general good agreement with previous works regarding fluoroargentates [40–44]. Notice, however, that in our work the peaks tend to have a mixed symmetry, which can be attributed to the influence of the ligand orbitals, which depart strongly from D_{4h} symmetry as discussed in Sec. II D.

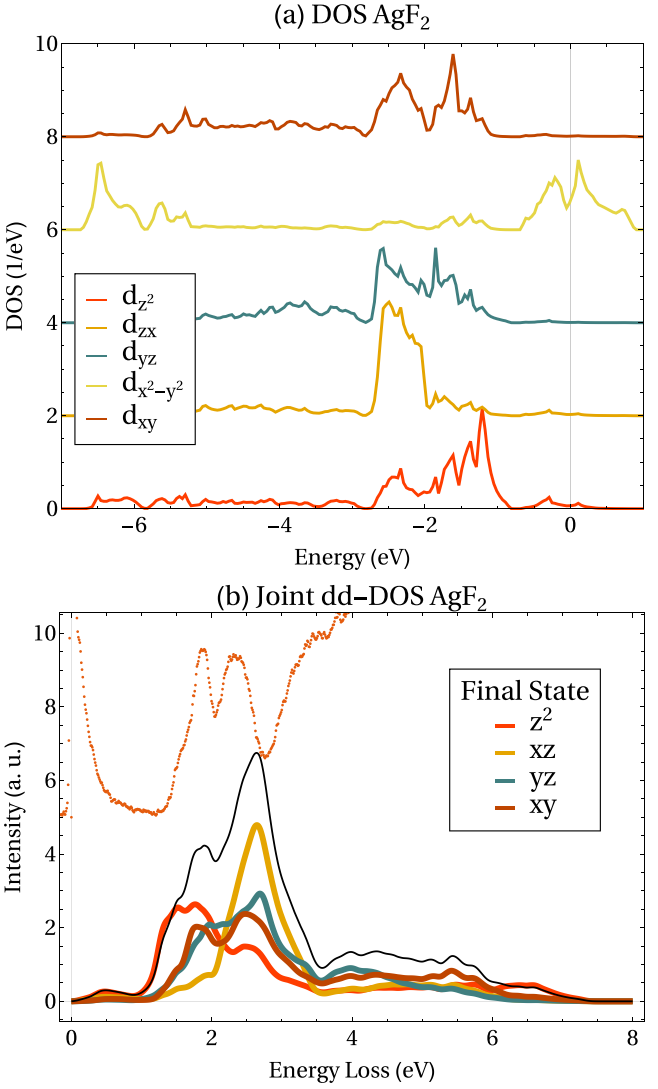

FIG. 5. (a) DOS of AgF_2 projected on Ag d orbitals from the unpolarized DFT computations. (curves have been shifted by 2 eV for clarity). The Fermi level is at zero energy. (b) Joint DOS between the unoccupied DOS of $d_{x^2-y^2}$ character and occupied DOS of different character representing dd transitions of a hole from the half-filled $d_{x^2-y^2}$ to a final state (labeled by the final state) character. The thin black line is the average of the different contributions. The dotted line is the experimental RIXS data.

Being the compound an insulator, it may appear natural to describe it with a DFT + U method [45] and an antiferromagnetic ground state as a starting point. Instead, our computation of dd transitions neglects the Hubbard U. This is not important here because dd excitations are charge neutral, i.e., an electron is taken from one-orbital and put in another orbital so that the Hubbard U does not play an important role.

The nonmagnetic computation, includes only shifts due to the ligand and crystal fields, which are the relevant ones. Instead, a DFT + U computation would include an additional large U shift from the outset in a mean-field manner, spoiling the agreement.

D. Comparison with cluster computations

An alternative description of the excitations, which emphasizes the local character, can be obtained with the cluster model presented in Sec. II D. Figure 6 shows the energy levels of the one-hole configuration of the cluster for AgF_2 and a cuprate [26]. The dashed lines on the left (right) of each panel are the d^9 ($d^{10}\underline{L}$) configurations. Each left-right pair of a given symmetry produces a bonding and antibonding level upon hybridization shown with the full lines. Notice that because we are showing hole energies, the bonding (antibonding) states are at high (low) energies. Energies are measured with respect to the x^2-y^2 ground state, so the vertical scale represents the energy of transitions to the different excited states. In addition, following Ref. [46] the energy of the ground state has been lowered by J, the magnetic stabilization energy due to the interaction with the neighbors. We have added one time J and not $2J$ since we have broken bonds with the neighbors while Ref. [46] considered a cluster with five Cu's and excited ferromagnetic alignment of spins.

The first striking difference between cuprates and AgF_2 is that the $d^{10}\underline{L}$ configurations have much smaller splittings in the fluoride [cf. Figs. 6(a), 6(b)]. This is in part a consequence of smaller F-F hoppings [14]. Optimized p Wannier orbitals have large crystal fields splittings parametrized by $\varepsilon_p(m)$ in Eq. (1), but they get averaged out when projected on the d-symmetrized states. Notice that in the case of cuprates, T_{pp} lowers the energy of the x^2-y^2 ligand orbital while the hybridization with the $d_{x^2-y^2}$ rises it, resulting in a bonding x^2-y^2 orbital at 4.8 eV slightly above the yz and xz orbitals. In the case of AgF_2, the lowering effect of T_{pp} is almost absent, so the x^2-y^2 bonding orbital is at much higher energies. The crossing with the other bonding levels as covalency is increased can be visualized in the Tanabe-Sugano diagram of Fig. 6(c) (top yellow line).

1. *dd* transitions

As a reference, we first discuss the case of cuprates for which we used one of the parameter sets considered by Eskes *et al.* for CuO in Ref. [26] and reproduced in Table II (labeled as Local in the La_2CuO_4 sector). The parameter Δ corresponds to the value quoted by Eskes *et al.* using a slightly different definition, namely, $\Delta - T_{pp}/5 = 2.2$ eV. From Fig. 6(b) we see that this set of parameters gives a quite good estimate of dd transition energies. As a bonus, this analysis suggests that the main structure seen in RIXS near 5 eV is a charge transfer transition from the ground state of mainly $d_{x^2-y^2}$ character to a hole in a combination of ligand orbitals with yz or xz symmetry. This is the lowest-energy pd transition within the cluster so its referred to as a local charge-transfer transition.

The position and ordering of dd transitions predicted in Ref. [26] and partially reproduced in Fig. 6(b) was studied with the advent of RIXS two decades latter. A detailed analysis [47] of the angular dependence of RIXS matrix elements confirmed the ordering and provided a refinement of the energies. Using a more ionic parameters set with a larger fundamental gap (last column in Table II) do not produce a satisfactory agreement. We will come later to this important point. Notice that the parameters in Fig. 6(a) have been adjusted ad hoc to fit the experiment while no such adjustment has been done for Fig. 6(b), which yields a slightly less accurate agreement for dd excitations.

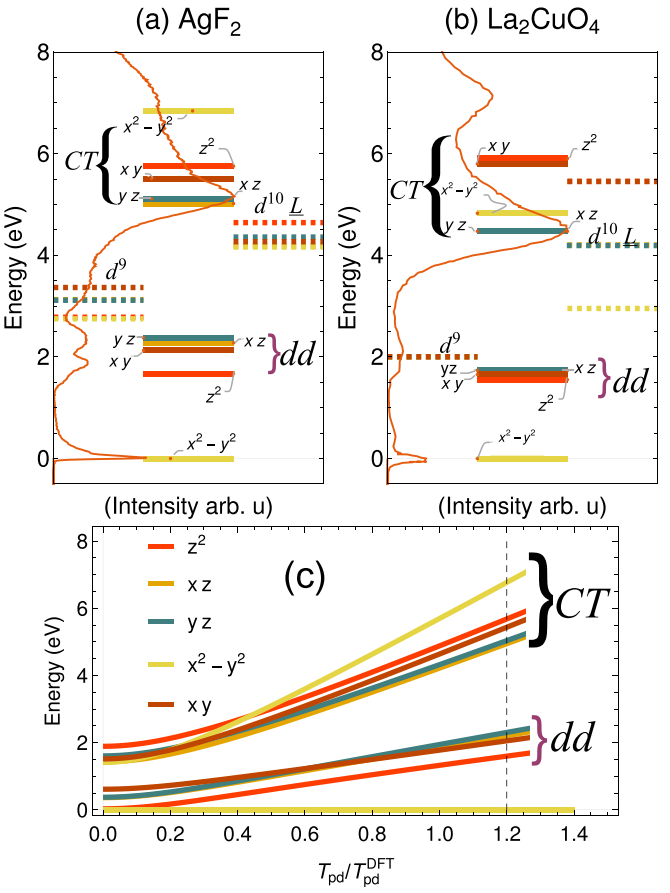

FIG. 6. Energy level diagram for one hole states in the clusters considered for (a) AgF_2 with $\Delta = 1.29$ eV and parameters from Table I with a 20% increase of the T_{pd} matrix elements and $J = 70$ meV as stabilization energy [46]. (b) La_2CuO_4 with $\Delta = 2.45$ eV and $J = 130$ meV. Dashed lines correspond to energies before hybridization in the d^9 configuration (left) and $d^{10}\underline{L}$ (right). Hybridization yields bonding and antibonding states (full lines). The ground state corresponds to the half-filled antibonding $d_{x^2-y^2}$, which was placed at zero energy so the vertical scale represent energies of transitions to states of majority d^9 character (i.e., dd transitions) around 2 eV and $d^{10}\underline{L}$ (i.e., charge-transfer transitions) at higher energy. RIXS spectra has been superposed for comparison. (c) shows the Tanabe-Sugano diagram for dd (lower lines set) and charge-transfer transitions (higher lines set). The position of excited states is measured with respect to the x^2-y^2 ground state and are plotted as a function of the renormalization of the T_{pd} matrix element with respect to the DFT value. The vertical line at $T_{pd}/T_{pd}^{DFT} = 1.2$ represents the value that was taken in our analysis to fit the experimental data. The magnetic stabilization energy of the $d_{x^2-y^2}$ state mentioned in the text has been omitted.

TABLE II. Comparison of parameter sets appropriate for local and nonlocal excitations and resulting fundamental gap for AgF_2 and La_2CuO_4. We also show the numbers of holes in the transition metal n_d. La_2CuO_4 parameter sets are taken from Ref. [26].

	AgF_2 (C_i)		La_2CuO_4 (D_{4h})	
	Local	Nonlocal	Local	Nonlocal
Δ	1.29	2.8	2.45	2.95
T_{pd}[a]	3.31	2.76	2.3	2.5
T_{pp}	0.11[b]	0.11[b]	1.25	1.0
F^0	6.48	6.48	6.81	7.31
F^2	8.19	8.19	11.41	11.41
F^4	6.80	6.80	7.31	7.31
$E_{\rm gap}$	1.54	2.25	1.27	1.8
n_d	0.60	0.73[c]	0.60	0.66

[a](x^2-y^2) symmetry.

[b]For AgF_2 we used crystal field parameters from Table I. For comparison we defined an effective $T_{pp} = [e_P(xz) + e_P(yz)]/2 - e_P(x^2 - y^2)$.

[c]Since the charge balance is determined by local transitions the physical value should be considered as the one computed with Δ in the Local column.

For AgF_2, we found that DFT parameters of Table I give a first ansatz for the position of RIXS structures including the DFT value for the charge-transfer parameter, $\Delta_{\rm DFT} = 1.29$ eV. However, this parameter set underestimates the energy of the dd transitions, which can be corrected by increasing the T_{pd} matrix elements by 20% as shown in the Tanabe-Sugano diagram of Figs. 6(c) and 6(a). In this way, the energies of the dd transitions match the experimental ones but, due to the low symmetry of the cluster, the lines should be understood as averages of the structures shown in Fig. 5(b) and a one-to-one correspondence of peaks and dd lines is oversimplified. On the other hand, this analysis suggests that also for the fluoride, the main peak in RIXS near 5 eV can be assigned to the local charge-transfer transition with a final state consisting in a hole in an orbital with xz or yz symmetry and mainly F character [cf. Fig. 6(a)].

The increase of T_{pd} should not be taken too seriously as it may just reflect longer-range hopping process from the $d_{x^2-y^2}$ and nonmagnetic stabilization terms of the x^2-y^2 ground state due to intercluster interactions beyond the magnetic correction introduced above. More importantly, increasing Δ with respect to the DFT value (i.e., increasing the ionicity) monotonously decreases the energy of dd transitions (i.e., worsening the agreement). We conclude that the description of dd transitions requires a quite covalent ground state in AgF_2. This is confirmed by the previous analysis of the joint DOS in Fig. 5, which is based on the same DFT computation.

2. Optical transitions

We now compare our theoretical analysis with the optical transitions. For a clean insulator, optical excitations measure the direct gap of the material. More precisely, the optical absorption may or may not show sharp transitions corresponding to particle-hole bound states (excitons), but should show an edge to a continuum of states. The threshold of the continuum corresponds to the minimum energy to separate an electron and a hole at an infinite distance and zero total momentum and defines the fundamental gap. We refer to these charge-transfer transitions as nonlocal. From the optical experiments, we obtained lower and higher bounds for the fundamental gap using two different methods: (i) a linear extrapolation of the edge giving a lower bound and (ii) a fit with a sharp edge broadened with a Gaussian distribution giving a higher bound. We estimate $E_{\rm gap} = 1.8 \pm 0.1$ eV for La_2CuO_4 and $E_{\rm gap} = 2.2 \pm 0.3$ eV for AgF_2.

Neglecting the band formation effects, we can estimate the fundamental gap as the minimum energy to extract an electron from one cluster and add it to another cluster, i.e., $E_{\rm gap} \equiv E_0(N+1) + E_0(N-1) - 2E_0(N)$. This energy corresponds also to the effective $U_{\rm eff}$ in a one-band model, which for cuprates provides a good description of the main charge-transfer absorption band in optics [48]. $E_0(N-1)$ corresponds to the ground state of the two-hole multiplet ($d^8 + d^9\underline{L}$), which is the Zhang-Rice state. The $N+1$ configuration corresponds to the filled shell so there is no multiplet but a unique state (d^{10}).

To compute the fundamental gap, we solved the many-body problem in the cluster using Lanczos exact diagonalization as implemented in the QUANTY package [49]. The Coulomb interaction in Eq. (2) was parametrized in terms of Slater integrals. For Cu we used the values corresponding to the Racah parameters of Ref. [26]. For Ag we took the values corresponding to the Racah parameters of Ref. [9] for F^2 and F^4 and took F^0 to be larger in view of the reduced screening expected in a fluoride with respect to an oxide [14]. Table II shows the resulting fundamental gap for the various parameters chosen. Both for AgF_2 and La_2CuO_4 the parameters that fit well the dd transitions (labeled Local) correspond to $E_{\rm gap}$ smaller than the one measured with optics. The effect is much stronger in AgF_2, which requires a quite small charge-transfer parameter to fit the dd transitions and yet has a larger experimental $E_{\rm gap}$ than cuprates. Notice that a small Δ does not imply that the local charge-transfer transitions are at small energy. Indeed, the local Δ represents the difference in energy between the levels before hybridization (difference between left and right multiplets with dashed lines in the top panels of Fig. 6). Instead, the local charge-transfer transition energies are set by the difference between hybridized levels (full lines in Fig. 6).

3. Nearest-neighbor repulsion and valence instability

We argue that the difference in Δ needed to fit optics (labeled Nonlocal) and RIXS (Local) reflects interactions beyond the on-site ones considered in Eq. (2). In particular, adding a nearest-neighbor repulsion between p and d orbitals, U_{pd}, renormalizes Δ in a different way for local (intracluster) and nonlocal (intercluster) charge-transfer excitations as shown schematically in Fig. 7. In the ionic limit, the effective Δ for local excitations ($d^9 \to d^{10}\underline{L}$) is $\Delta^{\rm loc} = \Delta_0 + U_{pd}$ while it enters as $\Delta^{\rm nl} = \Delta_0 + 2U_{pd}$ in the nonlocal excitations that define the fundamental gap. Here we define the difference of one-hole diagonal energies in the absence of Coulomb interactions, $\Delta_0 = \bar{\epsilon}_p^0 - \bar{\epsilon}_d^0$ and bar indicates average over the multiplet. Taking the difference of the first and second column

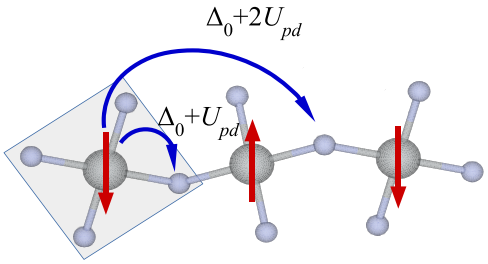

FIG. 7. Charge-transfer processes within the AgF_6 cluster (gray region) and to a distant fluorine.

Δ for each material, this implies a $U_{pd} \approx 0.5 \pm 0.2$ eV for cuprates (consistent with the accepted value) and $U_{pd} \approx 1.5 \pm 0.5$ eV for AgF_2, a value much larger than in cuprates.

In general, U_{pd} matrix elements will be orbital dependent, so our estimate above should be considered as a multiplet average. Coming back to the original p operators, the Hamiltonian for the nearest-neighbor Coulomb repulsion in one Ag-F bond can be written as

$$H_{\text{bond}} = \sum_{\nu,m} U_{pd}(\nu, m) d_\nu^\dagger d_\nu p_m^\dagger p_m.$$

We expect that also off-diagonal terms will be present, in particular

$$H'_{\text{bond}} = \sum_{\nu \neq \mu, m} W_{pd}(\nu, \mu, m) d_\nu^\dagger d_\mu p_m^\dagger p_m + \text{H.c.}$$

in which a hole in a p orbital induces a dd transition. This last operator naturally explains the RIXS activity for dd transitions at the ligand K edge and can be used to evaluate the cross section. We expect that U_{pd} and W_{pd} have a similar material dependence so the larger RIXS activity for dd transitions in AgF_2 with respect to the cuprates [cf. Figs. 6(a) and 6(b) in Fig. 6] is an indirect confirmation of the large intersite interactions.

So far we have used DFT to obtain spectral responses as it is customary done (Figs. 3 and 5). In general, these comparisons should be taken with a grain of salt as Kohn-Sham DFT [50] is a theory, which aims to find an auxiliary noninteracting system with the same density as the interacting system, and it is not warrant that the spectral functions of the auxiliary system will match the interacting ones. In the two cases above, correlations either not play an important role or tend to cancel, which partially explain the success.

The situation is different for the fundamental gap. The band structure of hybrid DFT computations [14] shows a smaller gap for AgF_2 than for La_2CuO_4 despite the fundamental gap in optics appears to have the opposite behavior. This should not be taken as a deficiency of DFT as this gap is just the gap of the auxiliary system constrained to be smaller to match the charge distribution of the interacting system. In other words, it is a measure of the strong covalency of the interacting system, not of its gap. Indeed, model computations [51] show that the Kohn-Sham gap in exact DFT is determined by the energy cost of neutral (i.e., local) excitations ($\Delta_0 + U_{pd}$ in our case) and not the nonlocal ones determining the fundamental gap $\Delta_0 + 2U_{pd}$. This gives further support to our finding that the DFT value for Δ has the right magnitude for describing neutral (local) transitions reconciling strong covalency [52] in the ground state with a large fundamental gap.

The large value of $U_{pd} \approx 1.5 \pm 0.5$ eV for AgF_2 poses a stability problem as it implies $\Delta_0 \approx -0.2 \pm 0.8$, which would make AgF_2 a negative charge transfer system as AgO. Taken literally and in the ionic limit, holes should populate the ligands as it occurs in formally d^9, silver oxide [9]. This can be avoided if one assumes that also intra- and intersite F-F Coulomb repulsions are present, which can stabilize the d^9 state. At present, the indeterminacies are too large, and it could be that Δ_0 is small but positive. In any case, our results point to AgF_2 being close to a charge-transfer instability. In this regard, it is very suggestive that besides the magnetic brown α-AgF_2 considered in this study, a metastable red-brown diamagnetic β phase has been reported [53], which has been interpreted in terms of a disproportionated (charge density wave) ground state. Although the structure of the β phase is not known, DFT computations [54,55] find a CDW polymorph very close in energy with respect to the usual antiferromagnetic phase, which also points to AgF_2 being at the verge of a charge-transfer instability.

V. CONCLUSIONS

We have measured the optical conductivity and resonant inelastic x-ray scattering spectra of AgF_2 to study its electronic excitations. We observe a charge transfer excitation between the F p bands and the Ag d bands peaking at about 3.4 eV in both optical conductivity and RIXS spectra. We resolve several dd excitations at 1.59, 1.86, and 2.33 eV from the RIXS spectra. We performed DFT and cluster calculations of the electronic structure, which allowed us to identify dd excitations and local charge-transfer transitions at high energy and a nonlocal charge-transfer transition determining the optical gap.

Using DFT and cluster computations, we provided estimates of the fundamental electronic parameters of this emerging quantum material, which are essential for future theoretical studies. The similarity between our data and that of the charge transfer insulator La_2CuO_4 is striking, but the subtle differences encode very interesting new physics. In particular, AgF_2 is predicted to be close to a charge-transfer instability due to a quite large value of U_{pd}. Interestingly, this parameter has been considered essential in some theories of cuprates [56] so a material with an enhanced U_{pd} can provide key clues to its role in determining the physics of cuprates.

The superconductivity in cuprates appears close to an insulating magnetic phase, while the same phenomenon in doped $BaBiO_3$ appears in proximity to the insulating CDW phase. Moreover, CDW instability along with a positive but small charger transfer energy have been realized in a recent study on K-doped $BaSbO_3$ [57] where the superconducting transition was shown to be higher than that of the same doping level in K-doped $BaBiO_3$. It is further postulated that the enhancement of T_c stems from the strong covalency of the metal-ligand bond, which is extremely relevant to our conclusions in view of the current results on AgF_2. Therefore, we expect a bright future in the search for doped [58] and hopefully superconducting [59] phases of AgF_2 that seems to combine both instabilities in the same material.

TABLE III. Explosives used for consecutive explosive compaction with their densities and detonation velocities, D.

Type	Explosive	Density [g/cm^3]	D [m/s]
A	Ammonal 2% (98% ammonium nitrate + 2% aluminum powder)	0.77	2600
B	Emulsion explosive (EmEx, mostly ammonium nitrate + fuel oil + water)	1.17	5300
C	Emulsion explosive (EmEx) + 20% 1,3,5-trinitro-1,3,5-triazinane (RDX)	1.25	5700

All the data related to this article are available in a dedicated space hosted by the University of Geneva [60].

ACKNOWLEDGMENTS

We acknowledge J. Teyssier for his help with the ellipsometry measurements. This work was supported by the Swiss National Science Foundation through projects 200020-179157 and CRFS-2-199368. W.G. acknowledges Polish National Science Centre (Maestro Grant No. 2017/26/A/ST5/00570). Z.M. acknowledges the financial support of the Slovenian Research Agency (research core funding No. P1-0045; Inorganic Chemistry and Technology). We acknowledge Diamond Light Source for providing the beam time under the Proposal No. NR24869 on the Beamline I21. P.B., G.G., and J.L. acknowledge support from MIUR Italian Ministry for Research through PRIN Projects No. 2017Z8TS5B and No. 20207ZXT4Z. J.L. acknowledges financial support from Regione Lazio (L. R. 13/08) under project SIMAP.

K.K. and J.G. contributed equally to this work. The sample was synthesized by Z.M. and shock compressed by W.T. and J.P. N.B., K.K., and J.G. carried out the optical spectroscopy measurements. Data analysis of the optical conductivity was done by N.B. and D.v.d.M. A.N. and K.Z. performed the RIXS measurements at the I21-RIXS beamline at Diamond Light Source. Data analysis of the RIXS data was carried out by A.N., K.Z. and G.G. R.P. P.B., and J.L. performed DFT and cluster calculations of the electronic structure. W.G. and J.L. conceived and supervised the entire project. N.B. and J.L. wrote the manuscript with inputs and comments from all coauthors.

APPENDIX A: SAMPLE PREPARATION PROCEDURE

A few-gram sample of AgF_2 has been placed inside of a 99.99% Cu container (Fig. 8), pressed manually using a copper cylinder, and the upper plug has been hammered into the container for even better compactness. All operations were carried out inside an argon-filled glove box.

Explosive compaction has been performed using three distinct types of explosives; their composition and results of measurements of the detonation velocity are presented in Table III. Consecutive explosions were carried out using the same container, but changing only parts 5 and 9 each time (cf. Fig. 8), due to their severe shock deformation.

Samples were undergoing explosive compaction in the following way:

(i) one sample underwent only type A explosion,

(ii) one sample underwent consecutive type A and B explosions,

(iii) one sample underwent consecutive type A, B, and C explosions.

Data on high-pressure behavior of silver fluorides up to 40 GPa [16] were used to calculate the compression shock curve of the crystalline AgF_2. The equation of state of a multicomponent medium (solid-gas) [61] was used to describe the physical properties of the porous AgF_2 samples loaded by a shock wave. To estimate the temperature in the shock-compressed sample, the dependence of specific heat on temperature for AgF_2 [14] was extrapolated to high temperatures. It was assumed that the entire energy of the shock

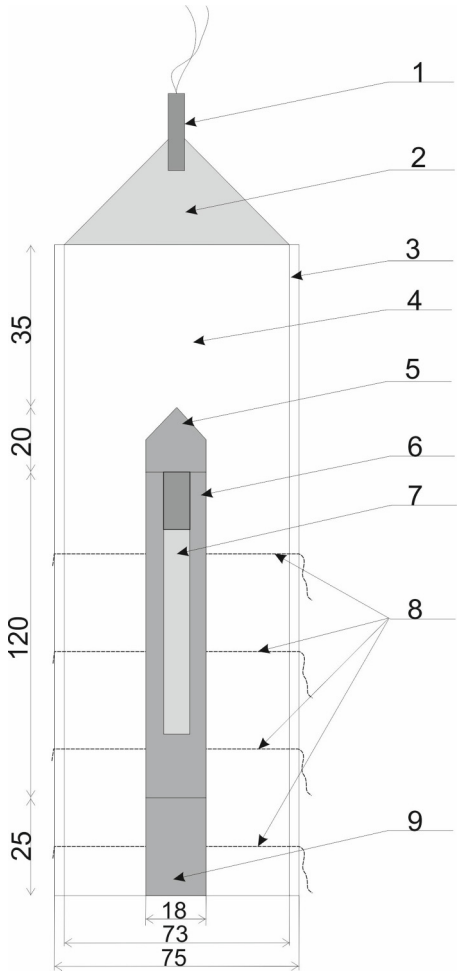

FIG. 8. Experimental setup for explosive compaction. 1 - electric detonator, 2 - plane wave generator, 3 - PVC tube, 4 - explosive, 5 - upper plug together with conical hat, 6 - container with compacted sample, 7 - compacted sample, 8 - short circuit sensors for measuring the detonation velocity, 9 - momentum trap. Dimensions are given in mm on the left-hand side.

compression of a porous sample is converted into heat, which causes the sample temperature to rise. The initial density of the samples was 3.14 g/cm^3. It was estimated that during the type A explosion, the maximum pressure in the sample was ca. 11 GPa, the maximum temperature was approximately 1500 °C and the density after loading was 5.1 g/cm^3. The explosion B in procedure (ii) resulted in substantially increased maximum pressure (63 GPa), but the temperature reached only 2100 K. The density of the samples after the loading B was 5.4 g/cm^3. In the type C explosion [procedure (iii)], the estimated pressure was 73 GPa and the temperature was 2000 K. Since the copper container did not explode, it was presumed that the pressure increase has substantially hindered the thermal decomposition of AgF_2 with the release of F_2 gas. Copper container was cut into pieces in an inert gas atmosphere. Indeed, visual inspection of the sample indicated that thermal decomposition and partial erosion of the container occurred only in the part of the sample adjacent to the container inner wall, while the inside of the sample cylinder was dark brown as typical for AgF_2. X-ray diffraction analysis revealed that the samples undergoing the procedure (iii) were nearly pure AgF_2, and the apparent density of the sample was approximately 95% of the crystallographic density; a small fraction of the sample might be amorphous.

APPENDIX B: ELLIPSOMETRY DATA

We measured the complex dielectric function using a Woollam VASE® spectroscopic ellipsometer in the energy range from 0.55–3.5 eV. The reflectivity ratio for p and s polarization is defined as

$$r_p/r_s = \rho = \tan(\Psi_{\text{ellip}})e^{i\Delta_{\text{ellip}}},$$

where Ψ_{ellip} and Δ_{ellip} are the parametric amplitude and phase difference components of the complex reflectivity ρ. We measured the r_p/r_s ratios at incident angles θ of 61° and 63° at selected temperatures of 300 K, 250 K, 226 K, 200 K, 176 K, 150 K, 100 K, 50 K, and 8 K. The corresponding $\Psi_{\text{ellip}}(\omega)$ and $\Delta_{\text{ellip}}(\omega)$ spectra for two angles of incidence measured at the lowest temperature are displayed in Fig. 9.

We fitted $\Psi_{\text{ellip}}(\omega)$ at two different angles of incidence (AOI) simultaneously following a similar but a separate fit to the $\Delta_{\text{ellip}}(\omega)$ spectra at two different angles of incidence using a Drude-Lorentz parametrization of $\epsilon(\omega)$. For the powder-pressed sample of AgF_2, we have used an isotropic model for $\epsilon(\omega)$. The confidence boundaries presented in Fig. 2 of the main text represent the possible range of σ_1 values between the two limits, i.e., a fit to Ψ_{ellip} data (2 AOI) and a fit to Δ_{ellip} data (2 AOI), thus reflecting our error bar for the reported results. A simultaneous fit to both Ψ_{ellip} and Δ_{ellip} was not possible to obtain under the use of a simple one-layer model of $\epsilon(\omega)$ for the AgF_2 sample. We assume that the discrepancy is due to the polycrystalline nature of the sample. Nevertheless, the impact of this discrepancy is mostly shown around the 1 eV absorption while the charge-transfer excitation is robust for both analysis procedures.

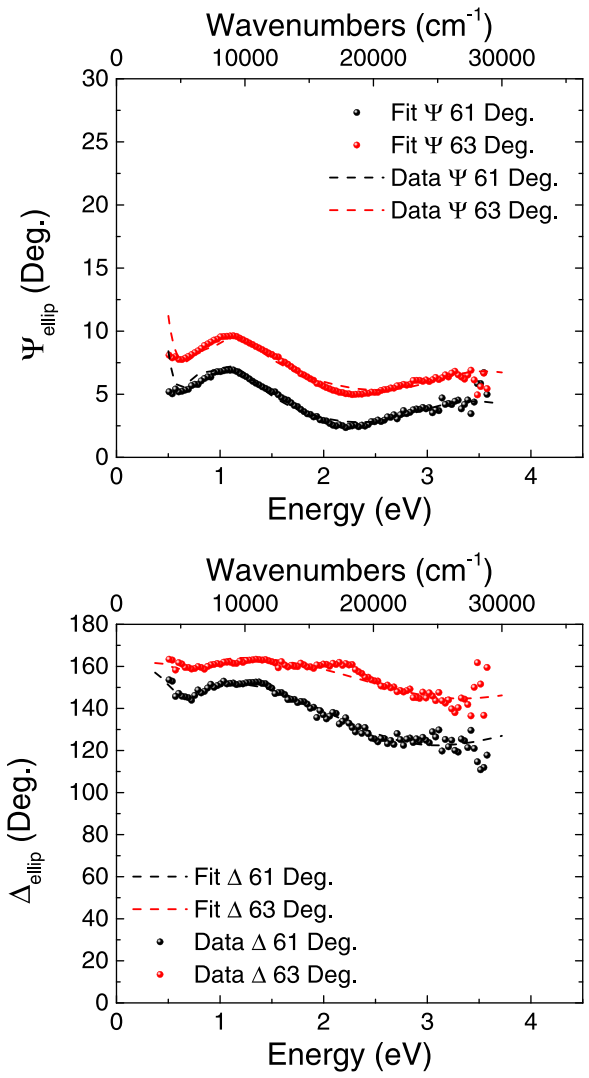

FIG. 9. The ellipsometric parameters Ψ_{ellip} and Δ_{ellip} as measured at temperature of 8 K for AOI of 61 (black spheres) and 63 (red spheres) degrees. The corresponding model fit as explained in the Appendix is shown in dashed lines.

To extract the optical conductivity directly from the r_p/r_s ratio, we have used the following pseudodielectric function:

$$\epsilon_{ps} = \sin^2(\theta)\left[1 + \tan^2(\theta)\left(\frac{1-\rho}{1+\rho}\right)^2\right],$$

where $\sigma = -i\nu 2\pi c\epsilon_0(\epsilon_{ps} - 1)$ is the optical conductivity in units of S/cm as shown in Fig. 2 for the real part. Here ν are wave numbers in cm^{-1}, c is the speed of light in vacuum in m/s and ϵ_0 is the vacuum permittivity in F/m.

[1] M. Cyrot, B. Lambert-Andron, J. Soubeyroux, M. Rey, P. Dehauht, F. Cyrot-Lackmann, G. Fourcaudot, J. Beille, and J. Tholence, Properties of a new perovskite oxyde Sr_2VO_4, J. Solid State Chem. **85**, 321 (1990).

[2] R. Viennois, E. Giannini, J. Teyssier, J. Elia, J. Deisenhofer, and D. V. der Marel, Two-dimensional orbital ordering in d^1 Mott insulator Sr_2VO_4, J. Phys.: Conf. Ser. **200**, 012219 (2010).

[3] F. Deslandes, A. Nazzal, and J. Torrance, Search for superconductivity in analogues of $La_{2-x}Sr_xCuO_4$: $Sr_{2-x}Ln_xVO_4$ (Ln=La, Ce, Pr, Nd, Eu), Physica C **179**, 85 (1991).

[4] F. Wang and T. Senthil, Twisted Hubbard Model for Sr_2IrO_4: Magnetism and Possible High Temperature Superconductivity, Phys. Rev. Lett. **106**, 136402 (2011).

[5] K. Wang, N. Bachar, J. Teyssier, W. Luo, C. W. Rischau, G. Scheerer, A. de la Torre, R. S. Perry, F. Baumberger, and D. van der Marel, Mott transition and collective charge pinning in electron doped Sr_2IrO_4, Phys. Rev. B **98**045107 (2018).

[6] X. Chen, T. Hogan, D. Walkup, W. Zhou, M. Pokharel, M. Yao, W. Tian, T. Z. Ward, Y. Zhao, D. Parshall, C. Opeil, J. W. Lynn, V. Madhavan, and S. D. Wilson, Influence of electron doping on the ground state of $(Sr_{1-x}La_x)_2IrO_4$, Phys. Rev. B **92**075125 (2015).

[7] A. de la Torre, S. M. Walker, F. Y. Bruno, S. Riccó, Z. Wang, I. Gutierrez Lezama, G. Scheerer, G. Giriat, D. Jaccard, C. Berthod, T. K. Kim, M. Hoesch, E. C. Hunter, R. S. Perry, A. Tamai, and F. Baumberger, Collapse of the Mott Gap and Emergence of a Nodal Liquid in Lightly Doped Sr_2IrO_4, Phys. Rev. Lett. **115**, 176402 (2015).

[8] D. Li, K. Lee, B. Y. Wang, M. Osada, S. Crossley, H. R. Lee, Y. Cui, Y. Hikita, and H. Y. Hwang, Superconductivity in an infinite-layer nickelate, Nature (London) **572**, 624 (2019).

[9] L. H. Tjeng, M. B. J. Meinders, J. van Elp, J. Ghijsen, G. A. Sawatzky, and R. L. Johnson, Electronic structure of Ag_2O, Phys. Rev. B **41**, 3190 (1990).

[10] S. E. McLain, M. R. Dolgos, D. A. Tennant, J. F. Turner, T. Barnes, T. Proffen, B. C. Sales, and R. I. Bewley, Magnetic behaviour of layered Ag fluorides, Nature Mater. **5**, 561 (2006).

[11] Z. Mazej, E. Goreshnik, Z. Jagličić, B. Gaweł, W. Łasocha, D. Grzybowska, T. Jaroń, D. Kurzydłowski, P. Malinowski, W. Koźminski, J. Szydłowska, P. Leszczyński, and W. Grochala, $KAgF_3$, K_2AgF_4 and $K_3Ag_2F_7$: important steps towards a layered antiferromagnetic fluoroargentate(II), CrystEngComm **11**, 1702 (2009).

[12] W. Grochala, Small changes, big consequences, Nature Mater. **5**, 513 (2006).

[13] D. Kurzydłowski, Z. Mazej, Z. Jagličić, Y. Filinchuk, and W. Grochala, Structural transition and unusually strong antiferromagnetic superexchange coupling in perovskite $KAgF_3$, Chem. Commun. **49**, 6262 (2013).

[14] J. Gawraczyński, D. Kurzydłowski, R. A. Ewings, S. Bandaru, W. Gadomski, Z. Mazej, G. Ruani, I. Bergenti, T. Jaroń, A. Ozarowski, S. Hill, P. J. Leszczyński, K. Tokár, M. Derzsi, P. Barone, K. Wohlfeld, J. Lorenzana, and W. Grochala, Silver route to cuprate analogs, Proc. Natl. Acad. Sci. USA **116**, 1495 (2019).

[15] T. Jaroń and W. Grochala, Prediction of giant antiferromagnetic coupling in exotic fluorides of AgII, Phys. Status Solidi (RRL) **2**, 71 (2008).

[16] A. Grzelak, J. Gawraczyński, T. Jaroń, D. Kurzydłowski, A. Budzianowski, Z. Mazej, P. J. Leszczyński, V. B. Prakapenka, M. Derzsi, V. V. Struzhkin, and W. Grochala, High-Pressure Behavior of Silver Fluorides up to 40 GPa, Inorg. Chem. **56**, 14651 (2017).

[17] D. Kurzydłowski and W. Grochala, Prediction of Extremely Strong Antiferromagnetic Superexchange in Silver(II) Fluorides: Challenging the Oxocuprates(II), Angew. Chem., Int. Ed. **56**, 10114 (2017).

[18] L. Braicovich, L. J. P. Ament, V. Bisogni, F. Forte, C. Aruta, G. Balestrino, N. B. Brookes, G. M. De Luca, P. G. Medaglia, F. Miletto Granozio, M. Radovic, M. Salluzzo, J. van den Brink, and G. Ghiringhelli, Dispersion of Magnetic Excitations in the Cuprate La_2CuO_4 and $CaCuO_2$ Compounds Measured Using Resonant X-Ray Scattering, Phys. Rev. Lett. **102**, 167401 (2009).

[19] L. Chaix, G. Ghiringhelli, Y. Y. Peng, M. Hashimoto, B. Moritz, K. Kummer, N. B. Brookes, Y. He, S. Chen, S. Ishida, Y. Yoshida, H. Eisaki, M. Salluzzo, L. Braicovich, Z.-X. Shen, T. P. Devereaux, and W.-S. Lee, Dispersive charge density wave excitations in $Bi_2Sr_2CaCu_2O_{8+\delta}$, Nature Phys. **13**, 952 (2017).

[20] K.-J. Zhou, A. Walters, M. Garcia-Fernandez, T. Rice, M. Hand, A. Nag, J. Li, S. Agrestini, P. Garland, H. Wang, S. Alcock, I. Nistea, B. Nutter, N. Rubies, G. Knap, M. Gaughran, F. Yuan, P. Chang, J. Emmins, and G. Howell, I21: an advanced high-resolution resonant inelastic X-ray scattering beamline at Diamond Light Source, J. Synchrotron Rad. **29**, 563 (2022).

[21] J. Pelliciari, Y. Huang, T. Das, M. Dantz, V. Bisogni, P. O. Velasco, V. N. Strocov, L. Xing, X. Wang, C. Jin, and T. Schmitt, Intralayer doping effects on the high-energy magnetic correlations in NaFeAs, Phys. Rev. B **93**, 134515 (2016).

[22] G. Kresse and J. Furthmüller, Efficient iterative schemes for ab initio total-energy calculations using a plane-wave basis set, Phys. Rev. B **54**, 11169 (1996).

[23] J. P. Perdew, K. Burke, and M. Ernzerhof, Generalized Gradient Approximation Made Simple, Phys. Rev. Lett. **77**, 3865 (1996).

[24] P. Fischer, G. Roult, and D. Schwarzenbach, Crystal and magnetic structure of silver difluoride-II. Weak 4d-ferromagnetism of AgF_2, J. Phys. Chem. Solids **32**, 1641 (1971).

[25] N. Marzari, A. a. Mostofi, J. R. Yates, I. Souza, and D. Vanderbilt, Maximally localized Wannier functions: Theory and applications, Rev. Mod. Phys. **84**, 1419 (2012).

[26] H. Eskes, L. H. Tjeng, and G. A. Sawatzky, Cluster-model calculation of the electronic structure of CuO: A model material for the high-T_c superconductors, Phys. Rev. B **41**, 288 (1990).

[27] J. P. Falck, A. Levy, M. A. Kastner, and R. J. Birgeneau, Charge-transfer spectrum and its temperature dependence in La_2CuO_4, Phys. Rev. Lett. **69**, 1109 (1992).

[28] J. P. Falck, J. D. Perkins, A. Levy, M. A. Kastner, J. M. Graybeal, and R. J. Birgeneau, Midinfrared electroreflectance in La_2CuO_{4+y}, Phys. Rev. B **49**, 6246 (1994).

[29] C. T. Chen, F. Sette, Y. Ma, M. S. Hybertsen, E. B. Stechel, W. M. C. Foulkes, M. Schluter, S.-W. Cheong, A. S. Cooper, L. W. Rupp, B. Batlogg, Y. L. Soo, Z. H. Ming, A. Krol, and Y. H. Kao, Electronic states in $La_{2-x}Sr_xCuO_{4+\delta}$ probed by soft-x-ray absorption, Phys. Rev. Lett. **66**, 104 (1991).

[30] S. Nakai, A. Kawata, M. Ohashi, M. Kitamura, C. Sugiura, T. Mitsuishi, and H. Maezawa, Core-exciton absorption in the F K absorption spectra of 3d transition-metal fluorides, Phys. Rev. B **37**, 10895 (1988).

[31] P. Olalde-Velasco, J. Jiménez-Mier, J. Denlinger, and W.-L. Yang, Atomic multiplets at the $L_{2,3}$ edge of 3d transition metals and the ligand K edge in x-ray absorption spectroscopy of ionic systems, Phys. Rev. B **87**, 245136 (2013).

[32] F. Bondino, M. Malvestuto, E. Magnano, M. Zangrando, M. Zacchigna, P. Ghigna, and F. Parmigiani, Overlap of Cu 3d and F 2p orbitals and low-energy excitations in $KCuF_3$ studied

by polarization-dependent x-ray absorption and emission spectroscopy, Phys. Rev. B **79**, 115120 (2009).

[33] V. Bisogni, L. Simonelli, L. J. P. Ament, F. Forte, M. Moretti Sala, M. Minola, S. Huotari, J. van den Brink, G. Ghiringhelli, N. B. Brookes, and L. Braicovich, Bimagnon studies in cuprates with resonant inelastic x-ray scattering at the O *K* edge. I. Assessment on La_2CuO_4 and comparison with the excitation at Cu L_3 and Cu *K* edges, Phys. Rev. B **85**, 214527 (2012).

[34] S. Uchida, T. Ido, H. Takagi, T. Arima, Y. Tokura, and S. Tajima, Optical spectra of $La_{2-x}Sr_xCuO_4$: Effect of carrier doping on the electronic structure of the CuO_2 plane, Phys. Rev. B **43**, 7942 (1991).

[35] G. A. Thomas, D. H. Rapkine, S. L. Cooper, S.-W. Cheong, A. S. Cooper, L. F. Schneemeyer, and J. V. Waszczak, Optical excitations of a few charges in cuprates, Phys. Rev. B **45**, 2474 (1992).

[36] S. L. Cooper, G. A. Thomas, A. J. Millis, P. E. Sulewski, J. Orenstein, D. H. Rapkine, S.-W. Cheong, and P. L. Trevor, Optical studies of gap, exchange, and hopping energies in the insulating cuprates, Phys. Rev. B **42**, 10785 (1990).

[37] J. D. Perkins, J. M. Graybeal, M. A. Kastner, R. J. Birgeneau, J. P. Falck, and M. Greven, Mid-infrared optical absorption in undoped lamellar copper oxides, Phys. Rev. Lett. **71**, 1621 (1993).

[38] D. N. Basov and T. Timusk, Electrodynamics of high-T_c superconductors, Rev. Mod. Phys. **77**, 721 (2005).

[39] S. Tajima, Optical studies of high-temperature superconducting cuprates, Rep. Prog. Phys. **79**, 094001 (2016).

[40] C. Friebel and D. Reinen, Ligandenfeld- und ESR-spektroskopische Untersuchungen zum JAHN-TELLER-Effekt des Ag2+-Ions in fluoridischer Koordination, Z. Anorg. Allg. Chem. **413**, 51 (1975).

[41] A. Monnier, A. Gerber, and H. Bill, The Jahn-Teller system Ag 2+ : NaF, an electron paramagnetic resonance and optical absorption study, J. Chem. Phys. **94**, 5891 (1991).

[42] J. A. Aramburu, M. Moreno, and M. T. Barriuso, How do the electronic properties of d 9 impurities depend on metal-ligand distances? Application to Ni +, Cu 2+ and Ag 2+ systems, J. Phys.: Condens. Matter **4**, 9089 (1992).

[43] R. Valiente, J. A. Aramburu, M. T. Barriuso, and M. Moreno, Electronic structure of Ag 2+ impurities in halide lattices, J. Phys.: Condens. Matter **6**, 4515 (1994).

[44] Z. Mazej, T. Michałowski, E. A. Goreshnik, Z. Jagličić, I. Arčon, J. Szydłowska, and W. Grochala, The first example of a mixed valence ternary compound of silver with random distribution of Ag(i) and Ag(ii) cations, Dalton Trans. **44**, 10957 (2015).

[45] V. I. Anisimov, M. A. Korotin, J. Zaanen, and O. K. Andersen, Spin bags, polarons, and impurity potentials in $La_{2-x}Sr_xCuO_4$ from first principles, Phys. Rev. Lett. **68**, 345 (1992).

[46] L. Hozoi, L. Siurakshina, P. Fulde, and J. Van Den Brink, Ab Initio determination of Cu 3d orbital energies in layered copper oxides, Sci. Rep. **1**, 65 (2011).

[47] M. M. Sala, V. Bisogni, C. Aruta, G. Balestrino, H. Berger, N. B. Brookes, G. M. de Luca, D. D. Castro, M. Grioni, M. Guarise, P. G. Medaglia, F. M. Granozio, M. Minola, P. Perna, M. Radovic, M. Salluzzo, T. Schmitt, K. J. Zhou, L. Braicovich, and G. Ghiringhelli, Energy and symmetry of dd excitations in undoped layered cuprates measured by Cu L_3 resonant inelastic x-ray scattering, New J. Phys. **13**, 043026 (2011).

[48] E. Dagotto, Correlated electrons in high-temperature superconductors, Rev. Mod. Phys. **66**, 763 (1994), 9311013.

[49] M. W. Haverkort, M. Zwierzycki, and O. K. Andersen, Multiplet ligand-field theory using Wannier orbitals, Phys. Rev. B **85**, 165113 (2012).

[50] W. Kohn and L. J. Sham, Self-Consistent Equations Including Exchange and Correlation Effects, Phys. Rev. **140**, A1133 (1965).

[51] V. Brosco, Z.-J. Ying, and J. Lorenzana, Exact exchange-correlation potential of an ionic Hubbard model with a free surface, Sci. Rep. **3**, 2172(2013).

[52] W. Grochala, R. G. Egdell, P. P. Edwards, Z. Mazej, and B. Žemva, On the covalency of silver-fluorine bonds in compounds of silver(I), silver(II) and silver(III), ChemPhysChem **4**, 997 (2003).

[53] C. Shen, B. Žemva, G. M. Lucier, O. Graudejus, J. A. Allman, and N. Bartlett, Disproportionation of Ag(II) to Ag(I) and Ag(III) in Fluoride Systems and Syntheses and Structures of $(AgF^+)_2AgF_4^-MF_6^-$ Salts (M = As, Sb, Pt, Au, Ru), Inorg. Chem. **38**, 4570 (1999).

[54] J. Romiszewski, W. Grochala, and L. Z. Stolarczyk, Pressure-induced transformations of $AgIIF_2$—towards an 'infinite layer' d9 material, J. Phys.: Condens. Matter **19**, 116206 (2007).

[55] K. Tokár, M. Derzsi, and W. Grochala, Comparative computational study of antiferromagnetic and mixed-valent diamagnetic phase of AgF_2: Crystal, electronic and phonon structure and p-T phase diagram, Comput. Mater. Sci. **188**, 110250 (2021).

[56] C. M. Varma, Considerations on the mechanisms and transition temperatures of superconductivity induced by electronic fluctuations, Rep. Prog. Phys. **75**, 052501 (2012).

[57] M. Kim, G. M. McNally, H.-H. Kim, M. Oudah, A. S. Gibbs, P. Manuel, R. J. Green, R. Sutarto, T. Takayama, A. Yaresko, U. Wedig, M. Isobe, R. K. Kremer, D. A. Bonn, B. Keimer, and H. Takagi, Superconductivity in (Ba, K)SbO_3, Nature Mater. (2022).

[58] S. Bandaru, M. Derzsi, A. Grzelak, J. Lorenzana, and W. Grochala, Fate of doped carriers in silver fluoride cuprate analogs, Phys. Rev. Materials **5**, 064801 (2021).

[59] A. Grzelak, H. Su, X. Yang, D. Kurzydłowski, J. Lorenzana, and W. Grochala, Epitaxial engineering of flat silver fluoride cuprate analogs, Phys. Rev. Materials **4**, 084405 (2020).

[60] N. Bachar, K. Koteras, J. Gawraczynski, W. Trzciński, J. Paszula R. Piombo, P. Barone, K.-J. Zhou, D. van der Marel, G. Ghiringhelli, A. Nag, J. Lorenzana, Z. Mazej, and W. Grochala, Data for "Charge-Transfer and *dd* excitations in AgF_2", Yareta, https://yareta.unige.ch/home/detail/f3989438-9fc3-4873-ba55-2a0a08a6e72f (2022).

[61] W. A. Trzciński, Theoretical assessment of the response of an explosive charge to the impact of a tungsten subprojectile, Materiały Wysokoenergetyczne / High Energy Materials **12**, 17 (2020).

Correction: The data availability statement and its source listing were missing and have been inserted.